X-ray Absorption Study of Structural Coupling in Photomagnetic Prussian Blue Analogue Core@Shell Particles

Daniel M. Pajerowski,*,[†] Bruce Ravel,[†] Carissa H. Li,[‡] Matthieu F. Dumont,[‡,§] and Daniel R. Talham[‡]

[†]National Institute of Standards and Technology, Gaithersburg, Maryland 20899, United States
[‡]Department of Chemistry, University of Florida, Gainesville, Florida 32611, United States

ABSTRACT: X-ray absorption spectroscopy experiments of core@shell, photomagnetic, and Prussian Blue analogue heterostructures obtain the local structure around the magnetic transition-metal ions before and after illumination. Two samples, containing nickel hexacyanochromate (Ni−Cr) and cobalt hexacyanoferrate (Co−Fe) in Ni−Cr@Co−Fe and Co−Fe@Ni−Cr geometries, were studied. Both materials display the well-known photoinduced valence tautomerism for Co−Fe, accompanied by a large change in cobalt to nitrogen distances. Furthermore, these experimental results show a structural coupling of the photoactive Co−Fe layer to the passive Ni−Cr layer. Finally, the strain across the heterostructured interface in Co−Fe and Ni−Cr containing core@shell models is investigated with simulations that use custom potentials derived from density functional theory calculations.
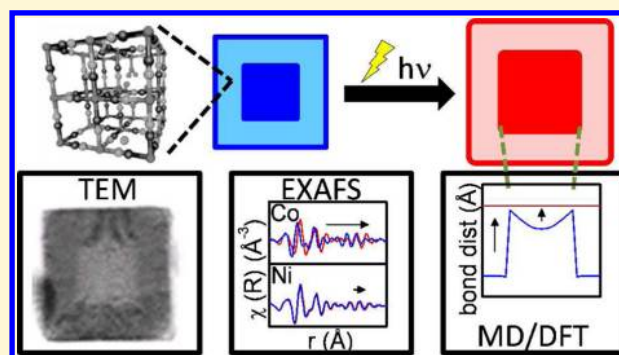
1. INTRODUCTION

Photoinduced magnetism, or sometimes photomagnetism, refers to the observed phenomenon whereby the magnetization of a material (the photomagnet) changes in response to applied light, and persistent photomagnetism is occasionally used to call attention to systems in which photoexcited states are robust even after ceasing illumination. Long-lived photomagnetism will make it possible to write data to a machine using light and later read back the information by detecting a magnetic field. However, before photomagnetism can become commercially viable for digital memory devices, the effects seen at low temperatures[1] must be reproduced at or near room temperature. Recently, there have been reports of photoinduced magnetism at elevated temperatures in heterostructured coordination polymers,[2−4] in a similar manner to the search for such a high temperature effect in a homogeneous material.[5−7] The study of heterostructures[2−4,8−11] are part of the current broader search for technological application of coordination polymers through manipulation of structure and morphology, which also includes nanocomposites,[12−14] tunable nanoscale structures,[15,16] and atomically layered systems.[17,18] In particular, core@shell metallocyanide particles, similar to those studied herein, are currently experiencing a surge due to progress in synthetic methods.[19,20]

Photomagnetic heterostructures are ostensibly made by coupling (in either layered-film[2,3] or core@shell geometry[4]) a pressure-sensitive magnet with a material having optically controllable structural deformation. Specifically, the high-T_C (60−90 K)[21] nickel hexacyanochromate (Ni−Cr) material that changes magnetization with applied pressure[22] can be combined with cobalt hexacyanoferrate (Co−Fe) compounds that change lattice constant with photoexcitation,[23−28] to show a large

reversible photoinduced decrease in magnetism at elevated temperatures for a Prussian Blue analogue (PBA) (see the coordination polymer in Figure 1). Based on the magnetic
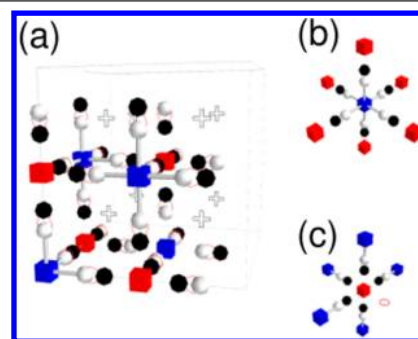

Figure 1. Prussian Blue analogue structure and local environments used in XAFS analysis. (a) The face-centered cubic Prussian Blue analogue structure consists of hexacyanometalate ions (blue boxes for the metal center, with white tubes showing the metal−carbon bond, white spheres for carbon, and black spheres for nitrogen) and the bridging transition-metal ions (red cubes). Hexacyanometallate ion vacancies are replaced with coordinating water molecules (red circles), and interstitial positions (white crosses) are occupied by either water molecules or alkali metal counterions. Representative local environment clusters are also shown in the hexacyanometalate site (panel b) and the coordinating transition-metal site (panel (c)). These local environments are utilized in the quantitative XAFS analysis that is presented later.

response, it was hypothesized that photoinduced structural distortions in the Co–Fe layer could couple to the Ni–Cr layer (applying a sort of pressure) to induce random anisotropy and thereby reduce the magnetism of the material. In core@shell particles, the interface between Co–Fe and Ni–Cr is expected to be a region of strain (see Figure 2).
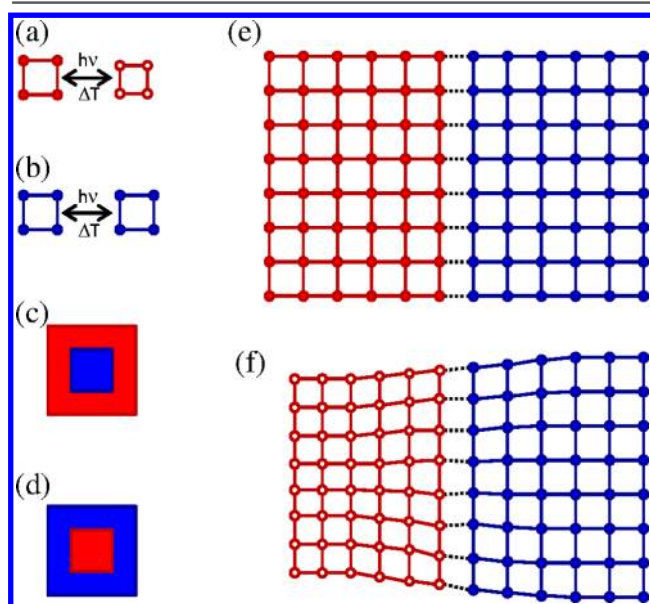

Figure 2. Coupling of photoinduced structural changes in core@shell particles. (a) The Co–Fe PBA undergoes a structural transformation that can be controlled using temperature or applied light. (b) The Ni–Cr PBA does not have an appreciable response to either of these stimuli. These materials may be incorporated into core@shell particles as either (c) Ni–Cr@Co–Fe or (d) Co–Fe@Ni–Cr. (e) At room temperature, or in the photoexcited metastable state at low temperature, Co–Fe PBA (red) and Ni–Cr PBA (blue) have similar lattice constants. (f) In the low-temperature ground state, there is a substantial mismatch between the contracted Co–Fe PBA (red) and Ni–Cr PBA (blue), and there is expected to be a region of strain in the vicinity of the interface before the particles may relax to their equilibrium lattice constants.

To test this hypothesized structural coupling of photoinduced distortions, we have performed X-ray absorption fine structure (XAFS) and X-ray absorption near-edge structure (XANES) spectroscopies. For materials such as the heterostructure in question, X-ray absorption spectroscopy (XAS) experiments are ideal, because of their ability to investigate local structure with elemental specificity, where techniques without elemental specificity can make deconvolution of response from different ions highly ambiguous. Previously, XAS has been used to better understand the bonding and structure of complex cyanide bridged networks[29−34] and even has played an essential role in elucidating the structural transitions in Co–Fe[24−28] and similar photomagnets.[35−37] Furthermore, to help with interpreting implications of our experimental observations, we have performed nanoscale simulations of Ni–Cr@Co–Fe and Co–Fe@Ni–Cr particles using custom potentials derived from density functional theory (DFT).

In the following article, we present analysis of Ni–Cr@Co-Fe and Co–Fe@Ni-Cr photomagnetic, core@shell particles using transmission electron microscopy (TEM) for sizes, infrared (IR) spectroscopy to confirm cyanide stretches in the PBA structure,[39] and energy-dispersive X-ray spectroscopy (EDX) to determine the chemical formula. These analyses then set the

stage for quantitative interpretation of XAS during illumination at low temperature, performed at the K-edge of the transition-metal ions present (Cr, Fe, Co, and Ni), with which approximate changes in oxidation-state populations due to photoexcitation are tracked using XANES, and structural changes due to photoexcitation are displayed in the XAFS. The documented large changes in the cobalt and iron environments of Co–Fe PBA after application of external light are observed,[24−28] and, remarkably, the nickel and chromium local environments within Ni–Cr PBA concomitantly change, albeit more subtly, because of a structural coupling of the layers. Finally, broader impacts of these results are discussed in the context of first-principles simulations.

2. MATERIAL AND METHODS[38]

2.a. Sample Characterization. The Ni–Cr@Co–Fe and Co–Fe@Ni–Cr core@shell particles were synthesized utilizing the previously reported procedures[4,8,9] that heterogeneously precipitate the shell material on core particles which are charge-stabilized in suspension by having been terminated in the cyanometallate precursor. Both EDX and TEM were conducted on a JEOL 2010F super probe at the Major Analytical Instrumentation Center at the University of Florida (UF), using acetone suspensions of the particles deposited onto 400 mesh copper grids with an ultrathin carbon film on a holey carbon support obtained from Ted Pella, Inc. For chemical formula determination, transition-metal content is obtained from EDX analysis, cyanide is fixed to be six-coordinated on the hexacyanometalate precursor, and interstitial cations are used to balance charge. Water molecules complete the coordination sphere of the divalent metals near $[Fe(CN)_6]^{3-}$ or $[Cr(CN)_6]^{3-}$ vacancies. A Thermo Scientific Nicolet 6700 spectrometer was used to record IR spectra using KBr pellets. Results of sample characterization are summarized below, and representative TEM images are shown in Figures 3a and 3b.
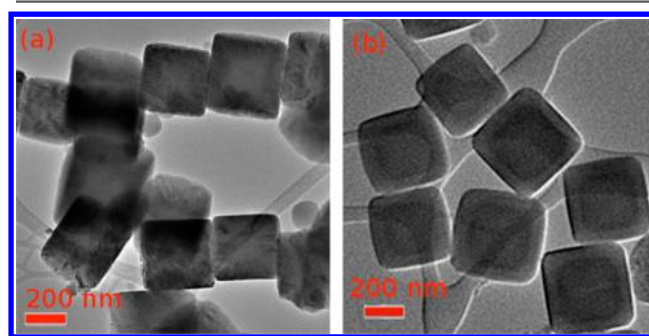

Figure 3. Particle structure. TEM images show a clear contrast between core and shell for both (a) Ni–Cr@Co–Fe (**1**) and (b) Co–Fe@Ni–Cr (**2**) core@shell particles.

$(K_{2.7}Ni_4[Cr(CN)_6]_{3.6}\cdot nH_2O@Rb_{2.1}Co_4[Fe(CN)_6]_{3.4}\cdot nH_2O)$ **Ni–Cr@Co–Fe (1).** TEM analysis revealed the following: particle size = 320 ± 20 nm, core size = 180 ± 20 nm; Ni–Cr:Co–Fe = 1.0:4.8. EDX analysis revealed a Co/Fe/Ni/Cr ratio of 46.27/35.45/9.66/9.61 (at. %), and Ni–Cr:Co–Fe = 1.0:4.8. IR analysis revealed peaks at 2123, 2163, and 2180 cm^{-1}.

$(Rb_{1.4}Co_4[Fe(CN)_6]_{3.1}\cdot nH_2O@ K_{2.4}Ni_4[Cr(CN)_6]_{3.5}\cdot nH_2O)$ **Co–Fe@Ni–Cr (2).** TEM analysis revealed the following: particle size = 410 ± 30 nm, core size = 320 ± 30 nm; Co–Fe:Ni–Cr ratio = 1.0:1.3. EDX analysis revealed a Co/Fe/Ni/Cr ratio of 22.55/17.58/32.05/27.82 (at. %), and Co–Fe:Ni–Cr = 1.0:1.4.

IR analysis revealed peaks at 2096, 2114, 2161, and 2176 cm^{-1}.

2.b. X-ray Absorption Methods. For these XAS measurements, <1 mg of each sample was mounted on a commercially available, clear, polyester adhesive tape, illumination was performed using a halogen light source, and temperature was controlled with a closed-cycle refrigerator. The XAFS and XANES data were collected at the National Synchrotron Light Source, on Beamline X23a2. The double crystal monochromator was operated with a pair of Si(311) crystals. A four-element Si-drift detector was used to detect fluorescence data. The detector count rate was adjusted to minimize the dead-time effects. Transmission data from reference metal foils, positioned after the sample and recorded simultaneously with each scan, were used for energy calibration. Background correction and normalization of spectra were done using Athena,[40] and the FEFF[41] interface Artemis[40] was used for quantitative fitting. Fourier transforms were performed with a k-range of 3 Å^{-1} to 8 Å^{-1}, with a k-weight of 2, and with a Hanning window ($dk = 1$), to fit data in direct space. The analysis programs utilize the XAFS equation in k-space:

$$\chi(k) = -S_0^2 \sum_i \left[\frac{N_i F_i(k)}{k R_i^2} \exp(-2\sigma_i^2 k^2) \exp\left(-\frac{2R_i}{\lambda(k)}\right) \right.$$
$$\left. \times \sin(2kR_i + \varphi_i(k)) \right] \qquad (1)$$

where k is the photoelectron wavenumber, S_0^2 the overall amplitude factor, N_i the degeneracy of scattering path i, F_i the effective scattering amplitude of path i, R_i the half-length of path i, σ_i^2 the Debye−Waller factor, λ the mean free path, and ϕ_i the phase shift of path i. Here, $k = [2m_e(E - E_0 - \Delta E_0)/\hbar^2]^{1/2}$ may also have the edge energy, E_0, adjusted to account for small differences, ΔE_0, between the experimental edge energy and its calculated value. The path degeneracies are fixed by the chemical formula and known crystal structure, and the overall amplitude factor is fixed to be 0.9. The effective scattering amplitudes, phase shifts, and mean free path were calculated using FEFF 6.00. The path lengths, energy shifts, and Debye−Waller factors were then extracted by fitting experimental data. Path lengths are parametrized using interatomic spacings within a model cluster. For each absorption edge, one energy shift parameter is used and there are three Debye−Waller parameters: one for paths only involving the nearest neighbor, another for paths involving next-nearest neighbors, and finally a factor for paths that include third-nearest neighbors. For cobalt and iron, two-phase fits were used when two oxidation states were present, with relative populations determined from XANES. It is worth noting that reduced residuals are possible by using models with more than the seven parameters we use, but we instead prefer to limit correlations between parameters.

2.c. Calculation Methods. To extract energies associated with changes in metal-to-metal distance and unit-cell angle, DFT calculations were performed using the GPAW[42,43] and ASE[44] codes. The experimentally determined anhydrous, neutral, and stoichiometric PBA unit cell was used as an initial condition for the first principles calculations. A real-space grid was used, with a nominal spacing of 0.15 Å that corresponds to a (64, 64, 64) grid. The LDA exchange-correlation functional with spin polarization was chosen with a $U = 3$ eV for onsite Coulomb repulsion and was applied to all d-electrons. The criterion of convergence for DFT calculations was applied without any symmetry constraints

to be <10^{-5} eV/electron in energy, <4 × 10^{-8} eV^2 for integrated eigenstate change, and <0.01 eV/Å for residual interatomic forces. Magnetic moments were initially set to the expected single-ion values based on the spectrochemical series, and were relaxed during optimization. Furthermore, for the Co−Fe material, additional calculations were performed using fixed moments in both the magnetic (denoted Co−Fe* in the context of potentials) and nonmagnetic (not shown) cases.

These DFT calculations were then fit to functions suitable to calculations on the molecular-dynamics scale (the nanoscale) and the pysic module[45] was used to supplement ASE. For bond stretching, potentials are fit to a harmonic approximation:

$$V(r) = \frac{1}{2}k_r(r - R_0)^2 + V_{r,0} \qquad (2)$$

where k_r is the coupling constant, R_0 the equilibrium position, r the relative position between the two metal centers, and $V_{r,0}$ an energy offset. Fits are performed from approximately ±3 Å around the minimum energy (Figure 4a), and the magnetic
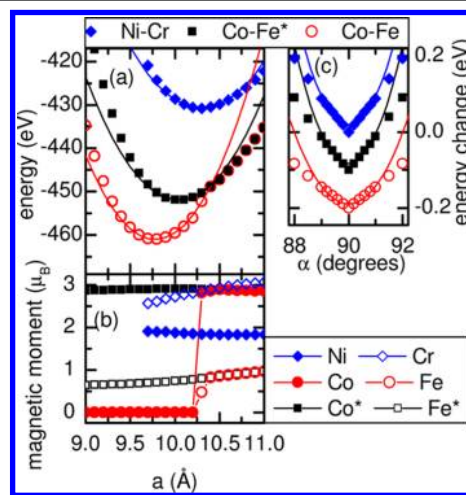

Figure 4. Bond deformation calculations. Bond-stretching: (a) Energy as a function of lattice constant a for Ni−Cr (blue diamonds (◆), k_r = 44.0 eV/Å^2), Co−Fe (red circles (○), k_r = 63.6 eV/Å^2), and fixed total moment Co−Fe* (black squares (■), k_r = 52.4 eV/Å^2). Lines are fits to eq 2. (b) Magnetic moment as a function of lattice constant for Ni−Cr (blue diamonds ((◇) Cr, (◆) Ni), Co−Fe (red circles ((○) Fe, (●) Co), and fixed total moment Co−Fe* (black squares ((□) Fe, (■) Co). Bond-bending: (c) Energy as a function of unit-cell angle, α, calculated at the equilibrium lattice constant for Ni−Cr (blue diamonds (◆), k_θ = 62.7 eV), Co−Fe (red circles (○), k_θ = 64.2 eV), and fixed total moment Co−Fe* (black squares (■), k_θ = 38.7 eV). Lines are fits to eq 3. Baseline energies are offset for the sake of clarity.

moments clearly show the Co−Fe phase transition (Figure 4b). In order to get a pairwise effective spring constant of a given unit cell, the fits for k_r are divided by three. The equilibrium metal-to-metal distance (from the cubic unit-cell constant) for nanoscale simulations was taken from experimental values to be ∼10.3 Å for magnetic Co−Fe*, ∼10.0 Å for nonmagnetic Co−Fe, and ∼10.3 Å for Ni−Cr.

For bond-bending, the potentials are fit to powers of cosines, such that

$$V(\theta) = -4k_\theta \left(\cos(\theta)^2 - \cos\left(\frac{\pi}{4}\right)^2 \right)^2 + V_{\theta,0} \qquad (3)$$

where k_θ is the bending constant, θ the angle between the three metal centers, and $V_{\theta,0}$ an energy offset. Angular fits are performed from 89° to 91°, and scaled by a factor of 3/8 for use in the nanoscale simulations as three-body potentials. The bond-bending calculations and fits are shown in Figure 4c.

The chosen potentials have desirable mathematical properties when it comes to performing a nanoscale simulation, as they are smooth, continuously differentiable, and possess only one minimum (in the region of study). Therefore, quasi-Newton optimization can be used, and a specifically limited memory implementation of the Broyden–Fletcher–Goldfarb–Shanno algorithm can be applied. Pragmatic considerations of our available computing power drove our choice of 64 000 object (40 × 40 × 40 cubes) calculations, and course-graining was performed to gain insight into larger particles. For course-graining, the same number of simulation objects are used, but to capture properties of larger systems, the space between the objects is mapped onto larger distances. Because of the nature of this mapping, the angular potentials of simulation objects effectively become less important than the distance-dependent potentials as larger systems are considered. The criterion of convergence for nanoscale simulations was based solely on maximal force and was set at 0.001 eV/Å. Curiously, although the potentials of the materials are ultimately very similar, these simulations show that the Co–Fe material is more resistive to compressive strain, while the Ni–Cr material is more rigid against unit-cell angle deformation.

3. RESULTS AND ANALYSES

3.a. X-ray Experiments. Samples were slowly cooled (at a rate of ~1 K/min) from 298 K to <20 K while monitoring the XANES of the Co K-edge, which is known to be strongly dependent on the oxidation state of the cobalt,[24−27] to verify the transition from Co^{2+} at room temperature to Co^{3+} at temperatures less than ~150 K. Once at base temperature, XAFS spectra were collected at the Ni, Cr, Co, and Fe K-edges with samples in a dark environment. Subsequently, the samples were photoexcited while monitoring the cobalt XANES (see Figure 5), to verify the low-temperature photoinduced transition from Co^{3+}
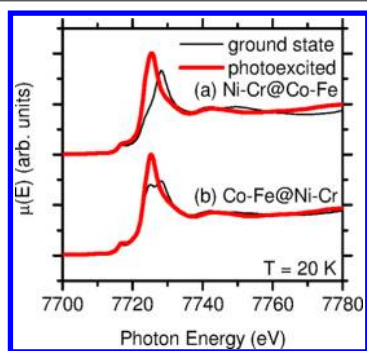

Figure 5. Co K-edge XANES spectra. XANES are shown for (a) Ni–Cr@Co–Fe (**1**) and (b) Co–Fe@Ni–Cr (**2**) before (thin, black line) and after (thick, red line) photoirradiation at $T \approx 20$ K. The charge transfer at the Co site is clearly seen by the increase in Co^{2+} resonance at ~7725 eV, at the expense of the Co^{3+} resonance at ~7728 eV.

back to Co^{2+}.[24] The Co edge was chosen, because it is the most sensitive to the transition, but there is also a more-subtle change in the Fe XANES and no clear change in the Ni or Cr edge energy, which supports robust Ni–Cr metal ion oxidation, with respect to the photoirradiation. After ~1 h, the change in Co

XANES was found to saturate. By assuming a complete conversion to divalent cobalt with irradiation, approximate cobalt oxidation state populations may be estimated from the XANES by profile fitting the absorption, as a function of energy, before irradiating the sample (μ_{dark}) and after irradiating the sample (μ_{light}). Explicitly, $\mu_{light} \equiv \mu_{Co^{2+}}$, $\mu_{dark} = n_{HS}\mu_{Co^{2+}} + (1 - n_{HS})\mu_{Co^{3+}}$, and the high-spin fraction (n_{HS}) is extracted by least-squares fitting while minimizing the curvature of $\mu_{Co^{3+}}$ at the Co^{2+} resonance between 7724 eV and 7726 eV. Then, the Ni–Cr@Co–Fe (**1**) particles in their low-temperature ground state have a Co^{2+}:Co^{3+} ratio of 0.1:0.9, which changes to 1.0:0.0 after excitation. Comparatively, the Co–Fe@Ni–Cr (**2**) particles have ground-state populations of 0.4:0.6 for the Co^{2+}:Co^{3+} ratio, which transform to 1.0:0.0 after illumination with light. While in the photoexcited state, XAFS spectra were again collected at the Ni, Cr, Co, and Fe K-edges.

The XAFS of Ni–Cr@Co–Fe (**1**) particles is shown in Figure 6. A rough understanding of the spectra can be understood through
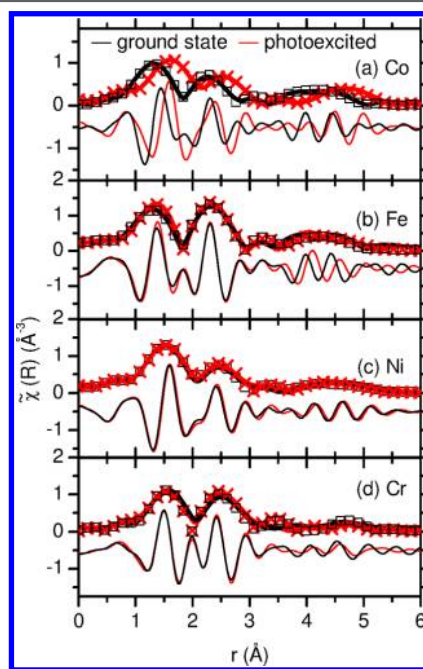

Figure 6. XAFS analysis of **1**, Ni–Cr@Co–Fe core@shell particles. Fourier transforms of K-edge XAFS oscillations with k^2 weight are shown for (a) Co, (b) Fe, (c) Ni, and (d) Cr. For each dataset, spectra prior to illumination (black line) are shown, along with spectra after illumination (red line) including the offset real part and magnitude of the absorption function. Fits to the ground-state (black squares, ■) and photoexcited states (red crosses, ✕) are also shown.

the loose, but certainly not rigorous, relationship of the real-space XAFS signal and a weighted radial distribution function. In Figure 6a, $\tilde{\chi}(R)$ shows three main peaks for the Co signal, and the paths contributing to these peaks are mainly due to Co ↔ N, Co ↔ C, and Co ↔ Fe, working from the nearest distance to the farthest distance; the entire chain moves with photoexcitation. Similarly, in Figure 6b, the Fe signal has three main peaks, which are mainly due to Fe ↔ C, Fe ↔ N, and Fe ↔ Co; photoexcitation has little effect on short paths but mostly on distance from Fe to Co. As such, the cobalt and iron data show the expected distinct change in Co–N bond length of ~0.170 Å,[24] because of the increased population of Co e_g^* antibonding orbitals for Co^{2+}, compared to Co^{3+}, with a subtle change in Fe–C bond length, because of the decreased

population of weakly bonding t_{2g} orbitals for Fe^{3+}, compared to Fe^{2+}. The Ni and Cr spectra strikingly also show changes in local structure with photoexcitation, with rigid Cr−C−N units and a slight elongation of the Ni−N distance, and the existence of these changes is most easily visualized by comparison of the real part of the absorption function from Figures 6c and 6d. The XAFS of Co−Fe@Ni−Cr (**2**) particles is shown in Figure 7, and similar
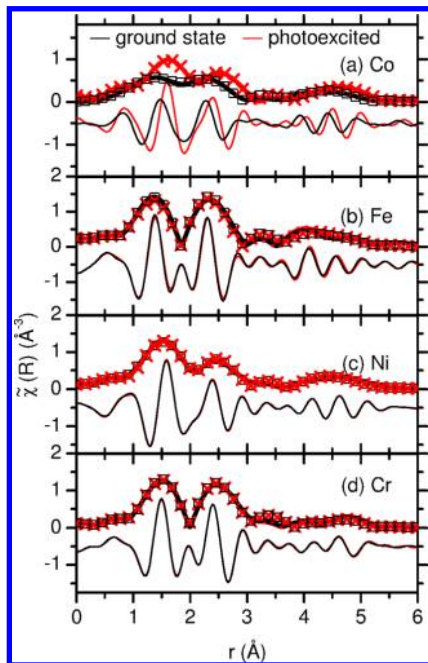

Figure 7. XAFS analysis of **2**, Co−Fe@Ni−Cr core@shell particles. Fourier transforms of K-edge XAFS oscillations with k^2 weight are shown for (a) Co, (b) Fe, (c) Ni, and (d) Cr. For each dataset, spectra prior to illumination (black line) are shown along with spectra after illumination (red line) including the offset real part and magnitude of the absorption function. Fits to the ground-state (black squares, ■) and photoexcited states (red crosses, ✕) are also shown.

features are seen as for the Ni−Cr@Co−Fe particles, excepting that any changes in the nickel environment are less than the

experimental resolution and the change in the Ni region of the Cr edge is very near the experimental resolution of our setup. In order to extract structural parameters, a quantitative analysis of the absorption data was performed using parameters described in the Materials and Methods section and the clusters shown in Figure 1b and 1c, with results summarized in Table 1 for Ni−Cr@Co−Fe and Table 2 for Co−Fe@Ni−Cr.

3.b. First-Principles Simulations. To better understand the observed differences in XAFS between Co−Fe@Ni−Cr (**1**) and Ni−Cr@Co−Fe (**2**) samples, first-principles simulations of how lattice parameters are influenced by the incorporation of the parent materials into the heterostructure were undertaken after the manner described in the Materials and Methods section. We explicitly consider three main core@shell parameters: (1) Co−Fe@Ni−Cr versus Ni−Cr@Co−Fe, (2) the relative amount of Ni−Cr to Co−Fe, and (3) the overall particle size. To this end, a series of Ni−Cr@Co−Fe particles (Table 3) and a series of Co−Fe@Ni−Cr particles (Table 4) were simulated. For naming the simulated samples introduced in this section, we adopt the practice of using bold type with ratios of core to shell in parentheses and, in some cases, an additional letter is appended to the name to delineate size. The states considered are the highly strained ground states (Figure 2f), where there is a large mismatch between nonmagnetic Co−Fe unit cell edge lengths (taken to be 10.0 Å) and Ni−Cr unit cell edge lengths (taken to be 10.3 Å). To parse the results, we have chosen to visualize the simulated systems in two ways: as a linescan through the center of the particle to display the depth dependence of interatomic distances, and as histograms of all unit-cell lengths and angles.

First, to investigate the effect of having the photoactive component in the core or shell and what happens when varying their proportions, a series of particles having the same approximate size (the same number of atoms) were considered. In Figures 8a, 8b, and 8c, unit-cell length and angle histograms show that the Ni−Cr@Co−Fe structures are strained, having peaks near the ground-state lattice constants that shift shape and proportion, depending on which material is present in a higher quantity. In addition, the distribution of unit-cell angles shows how strain is dispersed in the particles. Distorted bond lengths must compete with the cubic ground state and, therefore, the

Table 1. XAFS Fitting Results for 1, Ni−Cr@Co−Fe[a]

	Co K-edge						
	ΔE [eV]	$R_{Co−N/O}$ [Å]	$R_{Co−C}$ [Å]	$R_{Co−Fe}$ [Å]	$\sigma^2_{(Co−N)}$ [Å^2]	$\sigma^2_{(Co−C)}$ [Å^2]	$\sigma^2_{(Co−Fe)}$ [Å^2]
photoinduced state, P	1.45 ± 2.03	2.11 ± 0.01	3.27 ± 0.02	5.25 ± 0.05	0.009 ± 0.002	0.009 ± 0.003	0.017 ± 0.002
ground state, G	−10.99 ± 2.15	1.85 ± 0.02	3.04 ± 0.03	5.00 ± 0.03	0.008 ± 0.003	0.009 ± 0.003	0.016 ± 0.005
	Fe K-edge						
	ΔE [eV]	$R_{Fe−C}$ [Å]	$R_{Fe−N}$ [Å]	$R_{Fe−Co}$ [Å]	$\sigma^2_{(Fe−C)}$ [Å^2]	$\sigma^2_{(Fe−N)}$ [Å^2]	$\sigma^2_{(Fe−Co)}$ [Å^2]
photoinduced state, P	−8.97 ± 1.65	1.89 ± 0.02	3.06 ± 0.02	5.21 ± 0.03	0.003 ± 0.002	0.004 ± 0.003	0.019 ± 0.002
ground state, G	−10.65 ± 2.21	1.85 ± 0.02	3.05 ± 0.03	5.04 ± 0.03	0.000 ± 0.001	0.004 ± 0.002	0.020 ± 0.004
	Ni K-edge						
	ΔE [eV]	$R_{Ni−N/O}$ [Å]	$R_{Ni−C}$ [Å]	$R_{Ni−Cr}$ [Å]	$\sigma^2_{(Ni−N)}$ [Å^2]	$\sigma^2_{(Ni−C)}$ [Å^2]	$\sigma^2_{(Ni−Cr)}$ [Å^2]
photoinduced state, P	−7.51 ± 1.82	2.06 ± 0.02	3.20 ± 0.03	5.31 ± 0.05	0.004 ± 0.002	0.007 ± 0.005	0.021 ± 0.004
ground state, G	−8.33 ± 1.93	2.04 ± 0.02	3.17 ± 0.03	5.21 ± 0.06	0.004 ± 0.002	0.009 ± 0.005	0.021 ± 0.004
	Cr K-edge						
	ΔE [eV]	$R_{Cr−C}$ [Å]	$R_{Cr−N}$ [Å]	$R_{Cr−Ni}$ [Å]	$\sigma^2_{(Cr−C)}$ [Å^2]	$\sigma^2_{(Cr−N)}$ [Å^2]	$\sigma^2_{(Cr−Ni)}$ [Å^2]
photoinduced state, P	−3.36 ± 3.21	2.02 ± 0.03	3.25 ± 0.04	5.29 ± 0.07	0.002 ± 0.004	0.004 ± 0.003	0.036 ± 0.024
ground state, G	−3.31 ± 4.11	2.02 ± 0.03	3.25 ± 0.04	5.25 ± 0.09	0.002 ± 0.004	0.005 ± 0.004	0.025 ± 0.012

[a]Uncertainties come from the fitting algorithm and are one standard deviation of the residuals assuming an approximately normal residual distribution. Subscripts represent the paths associated with the parameters.

2590

dx.doi.org/10.1021/cm4042007 | *Chem. Mater.* 2014, 26, 2586−2594

Table 2. XAFS Fitting Results for 2, Co−Fe@Ni−Cr^a

	Co K-edge						
	ΔE [eV]	$R_{Co-N/O}$ [Å]	R_{Co-C} [Å]	R_{Co-Fe} [Å]	$\sigma^2_{(Co-N)}$ [Å^2]	$\sigma^2_{(Co-C)}$ [Å^2]	$\sigma^2_{(Co-Fe)}$ [Å^2]
photoinduced state, P	−0.13 ± 1.52	2.11 ± 0.02	3.25 ± 0.02	5.24 ± 0.03	0.011 ± 0.001	0.009 ± 0.003	0.018 ± 0.003
ground state, G	−6.30 ± 2.14	1.98 ± 0.03	3.09 ± 0.03	5.07 ± 0.03	0.023 ± 0.003	0.013 ± 0.003	0.022 ± 0.003

	Fe K-edge						
	ΔE [eV]	R_{Fe-C} [Å]	R_{Fe-N} [Å]	R_{Fe-Co} [Å]	$\sigma^2_{(Fe-C)}$ [Å^2]	$\sigma^2_{(Fe-N)}$ [Å^2]	$\sigma^2_{(Fe-Co)}$ [Å^2]
photoinduced state, P	−7.83 ± 1.83	1.88 ± 0.02	3.08 ± 0.02	5.20 ± 0.03	0.002 ± 0.002	0.004 ± 0.003	0.020 ± 0.002
ground state, G	−7.71 ± 2.03	1.87 ± 0.02	3.07 ± 0.03	5.14 ± 0.03	0.001 ± 0.001	0.003 ± 0.002	0.025 ± 0.004

	Ni K-edge						
	ΔE [eV]	$R_{Ni-N/O}$ [Å]	R_{Ni-C} [Å]	R_{Ni-Cr} [Å]	$\sigma^2_{(Ni-N)}$ [Å^2]	$\sigma^2_{(Ni-C)}$ [Å^2]	$\sigma^2_{(Ni-Cr)}$ [Å^2]
photoinduced state, P	−4.68 ± 2.01	2.06 ± 0.02	3.20 ± 0.03	5.32 ± 0.05	0.005 ± 0.002	0.006 ± 0.003	0.019 ± 0.004
ground state, G	−4.87 ± 2.02	2.06 ± 0.02	3.20 ± 0.03	5.32 ± 0.06	0.005 ± 0.002	0.006 ± 0.005	0.019 ± 0.004

	Cr K-edge						
	ΔE [eV]	R_{Cr-C} [Å]	R_{Cr-N} [Å]	R_{Cr-Ni} [Å]	$\sigma^2_{(Cr-C)}$ [Å^2]	$\sigma^2_{(Cr-N)}$ [Å^2]	$\sigma^2_{(Cr-Ni)}$ [Å^2]
photoinduced state, P	−3.54 ± 1.76	2.03 ± 0.02	3.23 ± 0.02	5.33 ± 0.06	0.001 ± 0.002	0.004 ± 0.002	0.027 ± 0.007
ground state, G	−3.69 ± 1.70	2.03 ± 0.02	3.22 ± 0.02	5.31 ± 0.06	0.001 ± 0.002	0.004 ± 0.002	0.029 ± 0.007

^{a}Uncertainties come from the fitting algorithm and are one standard deviation of the residuals assuming an approximately normal residual distribution. Subscripts represent the paths associated with the parameters.

Table 3. Simulated Ni−Cr@Co−Fe Particles^a

name	particle size [nm]	core size [nm]	core volume:shell volume
Ni−Cr@Co−Fe(6:1)	40	38	6:1
Ni−Cr@Co−Fe(1:1)	40	32	1:1
Ni−Cr@Co−Fe(1:7)	40	20	1:7
Ni−Cr@Co−Fe(1:7)L	400	200	1:7
Ni−Cr@Co−Fe(1:7)H	4 × 10^4	2 × 10^4	1:7

^{a}All quoted numbers are approximate, based on 1-nm unit-cell edges, in order to give an idea of simulation scale.

Table 4. Simulated Co−Fe@Ni−Cr Particles^a

name	particle size [nm]	core size [nm]	core volume:shell volume
Co−Fe@Ni−Cr(6:1)	40	38	6:1
Co−Fe@Ni−Cr(1:1)	40	32	1:1
Co−Fe@Ni−Cr(1:7)	40	20	1:7
Co−Fe@Ni−Cr(1:7)L	400	200	1:7
Co−Fe@Ni−Cr(1:1)L	400	320	1:1
Co−Fe@Ni−Cr(1:7)H	4 × 10^4	2 × 10^4	1:7

^{a}All quoted numbers are approximate, based on 1-nm unit-cell edges, in order to give an idea of simulation scale.

simulations with the biggest number of distorted bonds also have the largest angular spread. For Co−Fe@Ni−Cr simulations (Figures 8d, 8e, and 8f), the same general trends are present. However, the behavior is more complex than simply which material comprises more of the particle. By comparing samples having the same approximate chemical composition, but either Ni−Cr@Co−Fe or Co−Fe@Ni−Cr geometries, the emerging tendency seems to be toward a relaxed outermost shell, a strained phase in the vicinity of the interface, and a strained core. These trends are also seen in the linescan plots. An interesting feature explicitly shown in the linescans is how a smaller core actually increases the normally oriented shell bond lengths at the interface, and vice versa. This, perhaps counterintuitive, feature is a consequence not of the interface, but specific to the core@shell geometry. When the equilibrium lattice constants in the epitaxially bonded core are smaller than the equilibrium lattice

constants in the shell, the core is not only shrinking, but pulling away from the shell material, and there are regions where the comparable energy cost of shortening and elongating shell bonds will tip toward this seemingly capricious elongation, practically broadening the unit-cell length distribution, even while the mean distance shifts in the expected way. Again, the analogous discussion applies to the inverted geometry. To reiterate, the population of bonds that would undergo this type of strain is small and only show up in XAS as an increase in the standard deviation.

To gain insight about how particle size affects the structure of the core@shell systems, particles with fixed chemical formulas but different overall sizes were studied (see Figure 9). As anticipated, increasing the size of the particle reduces the relative proportion of strained bonds in the system. Specifically, the bonds in the core monotonically approach and finally reach their natural length as the particles get larger (see Figures 9a, 9b, 9d, and 9e). This result implies that there is a length scale of relaxation in the system, which can be estimated by considering the linescans of this simulation series (Figures 9a and 9d). Most relaxation happens after a few nanometers of an interface (whether in air or another PBA system), but more-subtle distortions are clear to tens of nanometers. It is important to remember that larger, computationally intractable systems were investigated by course-graining the simulations, and the data points in Figure 9 for different system sizes are not the same physical distance apart: the "∼400 nm" particle layer data points each scaled from ∼10 nm and the "∼40 μm" particle layer data points each scaled from ∼1 μm. Restated, a single simulation layer in a 400-nm particle is course-grained to actually contain 10 PBA unit-cell layers.

4. DISCUSSION

X-ray absorption spectroscopy (XAS) confirms that these Co−Fe/Ni−Cr core@shell particles possess the native photoinduced structural distortions of the Co−Fe compound. In the Ni−Cr@Co−Fe (**1**) sample, XAS further shows a subtle change in the Ni−Cr core structure that is related to the more drastic change in the Co−Fe layers. Conversely, the Co−Fe@Ni−Cr (**2**) sample shows much smaller changes in the Ni−Cr shell, which are near
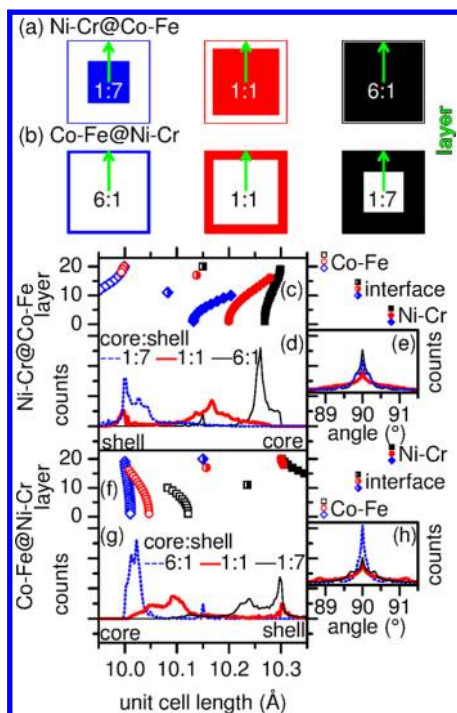
Figure 8. Simulations of ~40-nm core@shell particles with changing material proportions. Cross-sectional illustrations of (a) **Ni−Cr@Co−Fe(1:7)**, **Ni−Cr@Co−Fe(1:1)**, and **Ni−Cr@Co−Fe(6:1)** (from left to right), as well as (b) **Co−Fe@Ni−Cr(6:1)**, **Co−Fe@Ni−Cr(1:1)**, and **Co−Fe@Ni−Cr(1:7)** (also from left to right), display approximate layering constructions of the systems. Green arrows indicate the direction of particle layering, and the linescan vector that goes from the center of the particle to the outermost surface along a surface normal. Ni−Cr@Co−Fe: (c) The unit-cell length along a linescan through the simulated particle is shown for **Ni−Cr@Co−Fe(6:1)** (black squares (■) or thin black line), **Ni−Cr@Co−Fe(1:1)** (red circles (○) or thick red line), and **Ni−Cr@Co−Fe(1:7)** (blue diamonds (◆) or dotted blue line). These distances represent a small fraction of the total system, which is (d) histogrammed for the same simulation series, and (e) histograms are also shown for unit-cell angles. Co−Fe@Ni−Cr: (f) Linescans are shown for **Co−Fe@Ni−Cr(6:1)** (blue diamonds (◆) or dotted blue line), **Co−Fe@Ni−Cr(1:1)** (red circles (○) or thick red line), and **Co−Fe@Ni−Cr(1:7)** (black squares (■) or thin black line), as are the (g) unit-cell length histograms and (h) unit-cell angle histograms for this simulation series.

our experimental resolution, as the Co−Fe core expands with photoexcitation. However, even before photoexcitation of the Co−Fe@Ni−Cr, the Co−Fe core is strained toward having a significant population of longer length Co−Fe units. So, the XAFS shows a propensity of the core of both **1** and **2** to be strained toward the shell lattice constant in these samples. Of course, we must ask why this might be so.

We propose an explanation for these experimental findings by comparison with our simulations, which stand entirely independent of the XAS results. To begin, recall that the Ni−Cr@Co−Fe particles that we have synthesized are nominally 320 nm with a core:shell of ~1:5, and the synthesized Co−Fe@Ni−Cr particles are ~410 nm with a core:shell of ~1:1.4. The Ni−Cr@Co−Fe (**1**) sample is then quite similar to **Ni−Cr@Co−Fe(1:7)L**. On the other hand, the Co−Fe@Ni−Cr (**2**) sample does not compare easily to the already presented series of simulations, but can be compared to **Co−Fe@Ni−Cr(1:1)L**. To relate these simulations with experimental findings, we fit Gaussian peaks to the simulated unit cell length histograms while
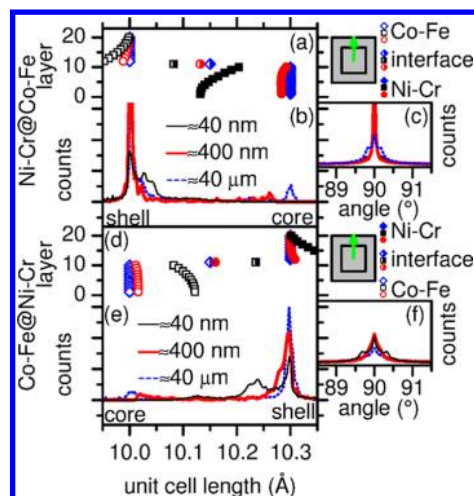

Figure 9. Simulations of 1:7 core:shell ratio particles with changing overall size. Ni−Cr@Co−Fe: (a) The scaled unit-cell length along a linescan through the simulated particle is shown for ~40 nm **Ni−Cr@Co−Fe(1:7)** (black squares, (■) or thin black line), ~400 nm **Ni−Cr@Co−Fe(1:7)L** (red circles or thick red line), and ~40 μm **Ni−Cr@Co−Fe(1:7)H** (blue diamonds, (◆) or dotted blue line). These distances represent a small fraction of the total system, which is (b) histogrammed for the same simulation series, and (c) histograms are also shown for unit-cell angles. Co−Fe@Ni−Cr: (d) Linescans are shown for ~40 nm **Co−Fe@Ni−Cr(1:7)** (black squares (■) or thin black line), ~400 nm **Co−Fe@Ni−Cr(1:7)L** (red circles, (○) or thick red line), and ~40 μm **Co−Fe@Ni−Cr(1:7)H** (blue diamonds or dotted blue line), as are the (e) unit-cell length histograms and (f) unit-cell angle histograms for this simulation series. The gray cross-section illustrates how the linescan is from the center of the particle to the outermost surface, along a surface normal.

dividing by two and average the metal-to-metal distances taken from XAFS (i.e., $(R_{Co-Fe} + R_{Fe-Co})/2$). These relationships are displayed in Figure 10. Strikingly, there is a high level of
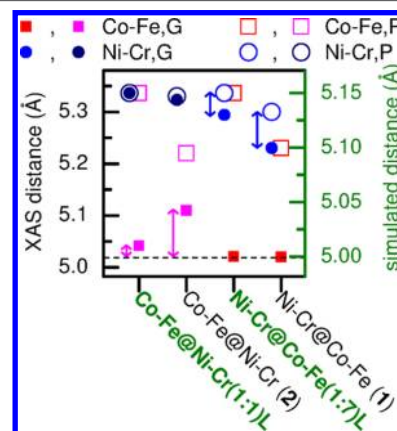

Figure 10. Comparison of average metal-to-metal distances extracted from XAS to similarly architectured simulations. "P" denotes the photoinduced state, in which Co−Fe metal ions have a larger equilibrium distance, and "G" denotes the ground state in which Co−Fe metal ions have a shorter equilibrium distance. The arrows shown call attention to the shift of Co−Fe metal ion distances in **Co−Fe@Ni−Cr(1:1)L** and **2**, as well as the shift in Ni−Cr metal ion distances for **Ni−Cr@Co−Fe(1:7)L** and **1**.

qualitative agreement between the simulations and experiments. Both **2** and **Co−Fe@Ni−Cr(1:1)L** show minimal change between photoexcited and ground-state Ni−Cr distances, with

a Co−Fe core, slightly shifted to a larger volume due to the influence of the longer bonds in the Ni−Cr shell. On the other hand, **1** and **Ni−Cr@Co−Fe(1:7)L** show a significant compression of the Ni−Cr bonds in the ground state, whereas the Co−Fe bonds that represent the preponderance of the sample are barely perturbed on average. So, the relative strain depends mainly upon which material is present in greater proportion, but also on the details of the nanostructure, and the initially confusing reduction in Ni−Cr structural coupling for **2** is found to be consistent with this developing picture.

Thus, it emerges that strain in these PBA core@shell structures can be engineered to give rise to the desired physical properties. In the context of the high-T_C photomagnetic effect that originally drew attention to the system,[3] there are a few considerations if one assumes that magneto-elastic coupling is responsible for the phenomenon. For the Co−Fe layer, there should be a sufficient quantity of material that the bonds are not too highly strained in the ground state that the Co−Fe photoeffect is completely destroyed; already in the measured Co−Fe@Ni−Cr particles, the effect is drastically reduced, because of distortions that exist before photoexcitation. Optimization of the Ni−Cr is less clear, because the precise nature of the magneto-elastic coupling has not yet been elucidated. However, it is likely that an optimal number of layers in similarly architectured films[3] is a compromise between having the largest change in strain operating over the magnetic coherence length. An important aspect of functional nanostructure engineering is the need to understand the mechanical properties of the constituents, which, in this case, are Prussian Blue analogues. Recently, a XAS study of nickel hexacyanoferrate showed there to be two regimes of pressure response for a PBA lattice and a point where magnetic circular dichroism is explained by a pressure induced loss of local symmetry.[46] More studies of this type on pure, bulk material will be absolutely essential to guide scientists in the quest to design and understand nanoarchitectured compounds.

It is worth noting that the simulated systems are simplistic by design, but real PBA systems have structural disorder and typically poor crystallinity. As such, the simulated results may be an upper-bound on rigidity in the PBA systems studied, and strain in real PBA systems may be relaxed more quickly into the background of the randomly distributed disorder. Furthermore, the lattice constants are dependent on the choice of alkali cation and stoichiometry, so compositions in Ni−Cr/Co−Fe nanostructures are frequently encountered with $a_{Co-Fe,G}$ = 9.9 Å, $a_{Co-Fe,P}$ = 10.33 Å, and a_{Ni-Cr} = 10.45 Å, which have an even larger lattice mismatch than simulated here, and are expected to have strain, even in the photoinduced state. In fact, our work does not allow Co−Fe under extreme strain to undergo a charge-transfer-induced spin-transition to change equilibrium lattice constants, as might be allowed in a more-complex simulation. Another interesting point to consider for future models is the reported presence of Ni−Fe at the Co−Fe/Ni−Cr interface, in a proportion that is dependent on synthesis protocol.[19]

It will be interesting to see how quantitatively core@shell systems that are designed with high crystallinity in mind reproduce the distortions predicted by the type of model presented in this work. Already, there are highly crystalline Ni−Cr/Co−Fe sub-50-nm nanostructures of core@shell and core@shell@shell geometries.[19] These Ni−Cr@Co−Fe particles of Dia and co-workers[19] have nanostructures that are similar to our ~40-nm **Ni−Cr@Co−Fe(1:7)** simulation (see Figures 8a, 8b, and 8c). Among other probes, they report X-ray diffraction (XRD) data, and from the Supporting Information of their

article, we extract a lattice parameter of $a_{Co-Fe,G}$ = 9.9 Å and broad peak giving a_{Ni-Cr} = 10.17 Å, whereas, for their bare Ni−Cr cores, we extract a value of a_{Ni-Cr} = 10.45 Å. Again, the qualitative agreement between model and experiment is strong.

Finally, it will be intriguing to see the manifestation of these types of structural couplings when probed with other techniques. For example, it was already seen that, in Ni−Cr/Co−Fe thin film heterostructures, XAFS and XRD are sensitive to different types of distortions to relax the strain in the system.[47] Thus, diffraction experiments are a logical next step. To really increase understanding of the interfacial versus average properties in coordination polymer heterostructures, it is likely that high-resolution electron microscopy can provide details about what types of defects are incorporated to help relax strain in these new nanostructured materials that are looking to be quite mechanically different than the more highly studied oxide and metal-based systems.

5. CONCLUSIONS

By utilizing X-ray absorption spectroscopy (XAS) and corroborating with first principles simulations, we have shown that photoinduced structural distortions in Co−Fe layers couple to Ni−Cr layers in Prussian Blue analogue coordination polymer heterostructures, suggesting the observed photomagnetic effects in these materials are related to the hypothesized structure−property relationships. In these PBA core@shell systems, the relative proportion of materials is a strong indicator of which component will experience higher strain, but details are dependent on the nanoarchitecture. Also, the simulations show the expected trend of bulk strain being relaxed as particles (and constituent layers) become larger. These findings give guidance to directed planning of core@shell systems, where the desired strain effects can be incorporated according to the goal of the fabricator. We expect that analogous effects to those observed in Ni−Cr/Co−Fe nanostructures may be designed for other heterostructured materials that include a photoinduced structural distortion and a pressure-sensitive layer, whether pertaining to magnetism, resistivity, or some other measurable. In an even broader sense, we hope this work provides direction to coordination polymer nanostructure researchers, whether they seek to make multifunctional materials and avoid strain effects or utilize strain to promote material synergy as in the current system.

■ AUTHOR INFORMATION

Corresponding Author
*E-mail: daniel@pajerowski.com.

Present Address
§The Sheikh Zayed Institute for Pediatric Surgical Innovation, Children's National Medical Center, Washington, DC 20010.

Notes
The authors declare no competing financial interest.

2593

dx.doi.org/10.1021/cm4042007 | Chem. Mater. 2014, 26, 2586−2594

■ REFERENCES

(1) Einaga, Y. *J. Photochem. Photobiol., C* **2006**, *7*, 69.

(2) Pajerowski, D. M.; Andrus, M. J.; Gardner, J. E.; Knowles, E. S.; Meisel, M. W.; Talham, D. R. *J. Am. Chem. Soc.* **2010**, *132*, 4058.

(3) Pajerowski, D. M.; Gardner, J. E.; Frye, F. A.; Andrus, M. J.; Dumont, M. F.; Knowles, E. S.; Meisel, M. W.; Talham, D. R. *Chem. Mater.* **2011**, *23*, 3045.

(4) Dumont, M. F.; Knowles, E. S.; Guiet, A.; Pajerowski, D. M.; Gomez, A.; Kycia, S. W.; Meisel, M. W.; Talham, D. R. *Inorg. Chem.* **2011**, *50*, 4295.

(5) Pejaković, D. A.; Kitamura, C.; Miller, J. S.; Epstein, A. J. *Phys. Rev. Lett.* **2002**, *88*, 057202.

(6) Yoo, J.-W.; Edelstein, R. S.; Lincoln, D. M.; Raju, N. P.; Epstein, A. J. *Phys. Rev. Lett.* **2007**, *99*, 157205.

(7) Bozdag, K. D.; Yoo, J.-W.; Raju, N. P.; McConnell, A. C.; Miller, J. S.; Epstein, A. J. *Phys. Rev. B* **2010**, *82*, 094449.

(8) Catala, L.; Brinzei, D.; Prado, Y.; Gloter, A.; Odile, S.; Rogez, G.; Mallah, T. *Angew. Chem., Int. Ed.* **2008**, *48*, 183.

(9) Presle, M.; Lemainque, J.; Guigner, J.-M.; Larquet, E.; Maurin, I.; Boilot, J.-P.; Gacoin, T. *New J. Chem.* **2011**, *35*, 1296.

(10) Talham, D. R.; Meisel, M. W. *Chem. Soc. Rev.* **2011**, *40*, 3356.

(11) Tricard, S.; Costa-Coquelard, C.; Mazerat, S.; Rivière, E.; Huc, V.; David, C.; Miserque, F.; Jegou, P.; Palacin, S.; Mallah, T. *Dalton Trans.* **2012**, *41*, 4445.

(12) Moore, J. G.; Lochner, E. J.; Ramsey, C.; Dalal, N. S.; Stiegman, A. E. *Angew. Chem., Int. Ed.* **2003**, *42*, 2741.

(13) Giorgetti, M.; Berrettoni, M.; Zamponi, S.; Kulesza, P. J.; Cox, J. A. *Electrochim. Acta* **2005**, *51*, 511.

(14) Aouadi, M.; Fornasieri, G.; Briois, V.; Durand, P.; Bleuzen, A. *Chem.—Eur. J.* **2012**, *18*, 2617.

(15) Ming, H.; Torad, N. L. K.; Chiang, Y.-D.; Wu, K. C.-W.; Yamauchi, Y. *CrystEngComm* **2012**, *14*, 3387.

(16) Lee, S.-H.; Huh, Y.-D. *Bull. Korean Chem. Soc.* **2012**, *33*, 1078.

(17) Yamada, R.; Tokoro, H.; Ozaki, N.; Ohkoshi, S.-i. *Cryst. Growth Des.* **2012**, *12*, 2013.

(18) Compain, J.-D.; Nakabayashi, K.; Ohkoshi, S.-i. *Inorg. Chem.* **2012**, *51*, 4897.

(19) Dia, N.; Lisnard, L.; Prado, Y.; Gloter, A.; Stéphan, O.; Brisset, F.; Hafez, H.; Saad, Z.; Mathionière, C.; Catala, L.; Mallah, T. *Inorg. Chem.* **2013**, *52*, 10264.

(20) Hu, M.; Belik, A. A.; Imura, M.; Yamauchi, Y. *J. Am. Chem. Soc.* **2013**, *135*, 384.

(21) Gadet, V.; Mallah, T.; Castro, I.; Verdaguer, M.; Veillet, P. *J. Am. Chem. Soc.* **1992**, *114*, 9213.

(22) Zentková, M.; Arnold, Z.; Kamarád, J.; Kavečanský, V.; Lukáčová, M.; Maťaš, S.; Mihalik, M.; Mitróová, Z.; Zentko, A. *J. Phys.: Condens. Matter* **2007**, *19*, 266217.

(23) Sato, O.; Einaga, Y.; Fujishima, A.; Hashimoto, K. *Inorg. Chem.* **1999**, *38*, 4405.

(24) Yokoyama, T.; Ohta, T.; Sato, O.; Hashimoto, K. *Phys. Rev. B* **1998**, *58*, 8257.

(25) Yokoyama, T.; Kiguchi, M.; Ohta, T.; Sato, O.; Einaga, Y.; Hashimoto, K. *Phys. Rev. B* **1999**, *60*, 9340.

(26) Bleuzen, A.; Lomenech, C.; Escax, V.; Villain, F.; Varret, F.; dit Moulin, C. C.; Verdaguer, M. *J. Am. Chem. Soc.* **2000**, *122*, 6648.

(27) dit Moulin, C. C.; Villain, F.; Bleuzen, A.; Arrio, M.-A.; Sainctavit, P.; Lomenech, C.; Escax, V.; Baudelet, F.; Dartyge, E.; Gallet, J.-J.; Verdaguer, M. *J. Am. Chem. Soc.* **2000**, *122*, 6653.

(28) Bleuzen, A.; Escax, V.; Ferrier, A.; Villain, F.; Verdaguer, M.; Munsch, P.; Itie, J.-P. *Angew. Chem.* **2004**, *116*, 3814.

(29) Giorgetti, M.; Berrettoni, M.; Filipponi, A.; Kulesza, P. J.; Marassi, R. *Chem. Phys. Lett.* **1997**, *275*, 108.

(30) Bonhoure, I.; Den Auwer, C.; dit Moulin, C. C.; Moisy, P.; Berthet, J.-C.; Madic, C. *Can. J. Chem.* **2000**, *78*, 1305.

(31) Hallmeier, K. H.; Sauter, S.; Szargan, R. *Inorg. Chem. Commun.* **2001**, *4*, 153.

(32) Glatzel, P.; Jacquamet, L.; Bergmann, U.; de Groot, F. M. F.; Cramer, S. P. *Inorg. Chem.* **2002**, *41*, 3121.

(33) Steen, W. A.; Han, S.-W.; Yu, Q.; Gordon, R. A.; Cross, J. O.; Stern, E. A.; Seidler, G. T.; Jeerage, K. M.; Schwartz, D. T. *Langmuir* **2002**, *18*, 7714.

(34) Garde, R.; Villain, F.; Verdaguer, M. *J. Am. Chem. Soc.* **2002**, *124*, 10531.

(35) Yokoyama, T.; Tokoro, H.; Ohkoshi, S.-i.; Hashimoto, K.; Okamoto, K.; Ohta, T. *Phys. Rev. B* **2002**, *66*, 184111.

(36) Yokoyama, T.; Okamoto, K.; Ohta, T.; Ohkoshi, S.-i.; Hashimoto, K. *Phys. Rev. B* **2002**, *65*, 064438.

(37) Ma, X.-D.; Toshihiko, Y.; Hozumi, T.; Hashimoto, K.; Ohkoshi, S.-i. *Phys. Rev. B* **2005**, *72*, 094107.

(38) Certain commercial equipment, instruments, or materials are identified in this paper to foster understanding. Such identification does not imply recommendation or endorsement by the National Institute of Standards and Technology, nor does it imply that the materials or equipment identified are necessarily the best available for the purpose.

(39) Buser, H. J.; Schwarzenbach, D.; Petter, W.; Ludi, A. *Inorg. Chem.* **1977**, *16*, 2704.

(40) Ravel, B.; Newville, M. *J. Synchrotron Radiat.* **2005**, *12*, 537.

(41) Rehr, J. J.; Zabinsky, S. I.; Albers, R. C. *Phys. Rev. Lett.* **1992**, *69*, 3397.

(42) Mortensen, J. J.; Hansen, L. B.; Jacobsen, K. W. *Phys. Rev. B* **2005**, *71*, 035109.

(43) Enkovaara, J.; Rostgaard, C.; Mortensen, J. J.; et al. *J. Phys.: Condens. Matter* **2010**, *22*, 253202.

(44) Bahn, S. R.; Jacobsen, K. W. *Comput. Sci. Eng.* **2002**, *4*, 56.

(45) http://thynnine.github.io/pysic/index.html.

(46) Cafun, J.-D.; Lejeune, J.; Itié, J.-P.; Baudelet, F.; Bleuzen, A. *J. Phys. Chem. C* **2013**, *117*, 19645.

(47) Pajerowski, D. M.; Zakrzewski, B. M.; Ravel, B. *Thin Solid Films* **2012**, *526*, 34.